Calculation of tip enhanced Raman scattering caused by nanoparticle plasmons acting on a molecule placed near a metallic film

Pavel I. Geshev
Institute of Thermophysics of Russian Academy of Sciences, Lavrentyev Avenue 1, 630090 Novosibirsk, Russia and Novosibirsk State University, Pirogova Street 2, 630090 Novosibirsk, Russia

Ulrich Fischer and Harald Fuchs
Westfälische Wilhelms-Universität, Wilhelm-Klemm-Straße 10, 48149 Münster, Germany

(Received 13 August 2009; revised manuscript received 22 December 2009; published 29 March 2010)

Light scattering in an axially symmetric composite system of a nanoparticle, an oscillating dipole and a metal film (covering a dielectric support) is considered. Nanoparticle and dipole are placed on the axis of symmetry. The axially oriented dipole is situated between film and nanoparticle. The field-enhancement factor at the position of the dipole and dipole radiation is calculated on the basis of Maxwell's equations, reduced by Green's functions to a system of boundary integral equations. The total enhancement of the light scattering, which is a product of the enhancement of the field intensity and the dipole radiation, depends on many parameters: the wavelength of light, the metal permittivity, film thickness, geometry of the nanoparticle, angle of incidence of the laser beam, but most strongly on the distance between the nanoparticle and film surface. According to our calculations, the total enhancement factor for Raman radiation can reach huge values in the order of $10^{10}-10^{11}$. The angular spectrum of the radiating dipole is derived and the accuracy of calculations is checked by the optical theorem of reciprocity.

DOI: 10.1103/PhysRevB.81.125441 PACS number(s): 68.37.Uv

I. INTRODUCTION

Coherent oscillations of the free-electron gas inside metallic nanoparticles cause an enhanced electric field near the particle surface. It is the main reason for phenomena like surface and tip enhanced Raman scattering [SERS (Refs. 1–10) and TERS (Refs. 11–17)], when under external illumination several molecules or even a single molecule (SM-SERS) placed in a narrow gap between two nanoparticles[8–10] or between a metallic surface and a scanning tunnel microscopy (STM) [or atomic force microscopy (AFM)] tip[11–17] produce an enhanced Raman radiation. It can be explained as antenna effect of two nanoparticles attached to the molecule (sandwichlike structure or dimer, according to Ref. 10). These antennas at first concentrate the incoming radiation and enhance the electric field at the molecule position. Then the same antennas enhance again and reradiate into space the Raman signal emanated by the molecule. For TERS the Raman enhancement factor measured in recent experiments[15] is about 10^6. It is much less than 10^{14} reported for SM-SERS experiments.[8,9] Because STM and AFM devices are among the major tools for the investigation and manipulation on the nanolevel, it is important to estimate the potential of TERS in a sense of single molecule spectroscopy.

The large enhancement in SM-SERS (SM-TERS) experiments can have several reasons. When a molecule is pressed between the tip and surface the electronic orbitals in the tip material and in a molecule can overlap and electron transfer can change and increase the Raman signal.[18] Usually, the contribution of this chemical enhancement factor is estimated to be small. This mechanism is not considered here. Our interest is focused on the electromagnetic (EM) mechanism of the SERS phenomenon, calculated on the basis of classic electromagnetic theory described by Maxwell's equations. Electromagnetic models of SERS at first were developed in a nonretarded approach,[4–6] then in partially retarded variants,[19,20] and also as full Maxwell models.[21–23] They explained many details in SERS and the intensity enhancement factors of order 10^5-10^7 are obtained in these papers. It must be noted that usually in these models the effects of an adjacent particle or surface were neglected.

An interesting idea to use an illuminated metallic nanoparticle as a detector in a configuration where the particle is scanned over a surface was suggested by Wessel.[24] Indeed, in calculations made by Takemori *et al.*[25] for a very small Ag sphere near an Ag surface (at gap 1 nm) values for the Raman enhancement factors of about 10^8 were obtained. The first experiments conducted by Fischer and Pohl[26] with spherical nanoshells and Inouye and Kawata[27] with metallic tip excited by light in a Kretschmann configuration[28] have really shown a large increase in the elastic scattering signal. It was an indication that the neighborhood of a metallic surface can increase the enhancement of Raman radiation of molecules adsorbed on a nanoparticle. One should also mention the paper of Xu *et al.*,[10] where not only the key idea of a dimer (two coupled nanoparticles) was formulated but also an enhancement factor of the Raman signal in the order of 10^{10} (at the gap 1 nm) was obtained theoretically for the dimer. Moscovits noted,[7] that the highest field enhancement can be met in gaps between closely spaced metal features in aggregated colloids or cold-deposited films.

From the first quasistatic models of SERS,[4–6] it is known that the Raman enhancement factor is proportional to the fourth power of the electric field at the position of the molecule. The main values to be calculated should be the maximally enhanced field (at the poles of the nanoparticle) and the fluxes of light energy scattered from the nanoparticle. The scattering system is depicted in Fig. 1, where the dipole

 ©2010 The American Physical Society

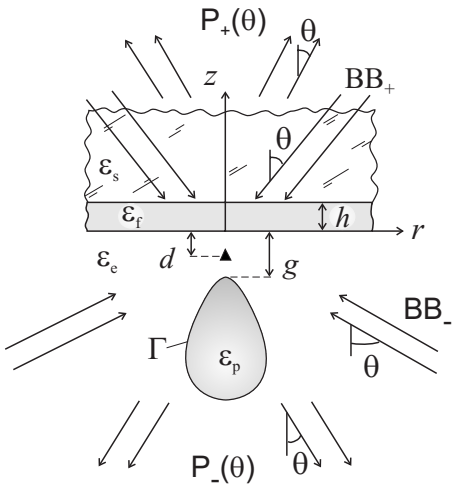

FIG. 1. Axial symmetrical scheme of a scattering system: a nanoparticle, a dipole (triangle), a thin film, a dielectric substrate, characteristic lengths (d, g, h), permittivities of media (ε_s, ε_e, ε_f, ε_p), illuminating Bessel light beams (BB), and enhanced dipole radiations $P(\theta)$ are shown. The contour of NP is signified by letter Γ.

(black triangle) and the nanoparticle (NP), placed together on the symmetry axes close to a layered medium, are shown. The dielectric support, film, lower semispace and NP have permittivities ε_s, ε_f, ε_e, and ε_p, respectively. NP's contour Γ and characteristic lengths d, g, and h, are designated in Fig. 1. Four light beams: two illuminating Bessel beams (BBs) (BB_+ *or* BB_) and the outgoing dipole radiation in two directions [$P_+(\theta)$ *and* $P_-(\theta)$] are indicated in Fig. 1. Plasmons excited in the NP and in the metallic film enhance the electric field at the dipole position. This is described by field-enhancement factors (FEFs): $\mathrm{FEF}_+(\theta)$ for BB_+ and $\mathrm{FEF}_-(\theta)$ for BB_. The introduced factors are calculated independently as solution of four problems. But thanks to the known feature called optical reciprocity some of them must be exactly proportional to each other: $\mathrm{FEF}_+(\theta) \propto P_+(\theta)$ and $\mathrm{FEF}_-(\theta) \propto P_-(\theta)$. This will be demonstrated in the paper.

A large enhancement occurs only for the exciting electric field polarized along the symmetry axis which can be arranged by a side illumination, but more effectively by a radially polarized Bessel beam.[29–32] It was shown, that in the focus of such a beam a strong electric field directed along the beam axis is produced. Similar radially polarized beams were used as illumination sources in theoretical models,[33–36] where the electric field enhancement[33,34] and radiation fluxes for nanoparticle and dipole[35] placed near a metallic semispace or a thin metal film[36] were calculated by the boundary element method.

The main motivation of our work is to find through extensive calculations the answer on the question: at what circumstances can we expect for TERS really huge enhancement factors? Here our previous work[36] is continued by dealing with: (1) a full description of the method of calculation; (2) metals other than silver (aluminum, gold); (3) "large" nanoparticles ~ 1 μm; (4) a derivation of the angular spectrum of the dipole radiation; and (5) a demonstration of the agreement of the results with the optical reciprocity theorem.

The paper is organized as follows. In Sec. II the Bessel beam passing through the layered medium and the radiation of a dipole placed near this medium are considered in the absence of a nanoparticle. In Sec. III the Green's functions and basic boundary integral equations (BIEs) are introduced and main enhancement factors for the electric field in a particle/surface gap and for the energy flux from the dipole are determined. In Sec. IV a total Raman radiation enhancement factor (REF) and two important relative enhancement factors for the local field and for the dipole radiation are introduced and the results are presented for nanobodies of various shapes and sizes. Sections V and VI contain the discussion and conclusion, respectively.

II. TWO TYPES OF LIGHT SOURCES: BESSEL BEAM AND RADIATING DIPOLE

A. Bessel beam illumination of a thin metal film covering a dielectric support

Let us consider a radially polarized light beam (Bessel beam or BB) propagating through the layered medium: dielectric/film/dielectric. Only axial symmetric and time harmonic solutions of Maxwell's equations are considered in a frequency domain [with time dependence $\exp(-i\omega t)$, where ω is the light frequency and t is time]. All coordinates are made dimensionless by the reduced wavelength of light $\lambda = \lambda/2\pi$. Maxwell's equations are used in the Gauss system of units. The external illumination must also have an axial symmetry and obey Maxwell's equations. One can build this external field by a superposition of solutions for the reflected and transmitted parts of the electromagnetic waves going through the dielectric and the metal film. The result is formulated for the azimuthal φ component of the magnetic field H_φ, the only nonzero magnetic field component for the light beam with a radial polarization of the electric field.

(1) For the case of a beam incident on the film from below (BB_ in Fig. 1)

$$H_e = H_0 J_1(r\sqrt{\varepsilon_e}\,\sin\,\theta)[e^{i\chi_e z} + R_- e^{-i\chi_e z}], \quad (z \le 0), \quad (1)$$

$$H_s = H_0 J_1(r\sqrt{\varepsilon_e}\,\sin\,\theta) T_- e^{i\chi_s (z-h)}, \quad (z \ge h), \quad (2)$$

$$R_- = \frac{\Lambda_{ef} - \Lambda_{sf} E^2}{1 - \Lambda_{ef}\Lambda_{sf} E^2}, \quad T_- = \frac{(1+\Lambda_{ef})(1-\Lambda_{sf})E}{(1-\Lambda_{ef}\Lambda_{sf}E^2)},$$

$$\Lambda_{ef} = \frac{\chi_e \varepsilon_f - \chi_f \varepsilon_e}{\chi_e \varepsilon_f + \chi_f \varepsilon_e}, \quad \Lambda_{sf} = \frac{\chi_s \varepsilon_f - \chi_f \varepsilon_s}{\chi_s \varepsilon_f + \chi_f \varepsilon_s}, \quad E = \exp(i\chi_f h), \quad (3)$$

where $J_1(\cdot)$ is the Bessel function, h is the film thickness, and the dimensionless axial wave vector components are:

$$\chi_e = \sqrt{\varepsilon_e}\,\cos\,\theta, \quad \chi_f = \sqrt{\varepsilon_f - \varepsilon_e \sin^2\,\theta}, \quad \chi_s = \sqrt{\varepsilon_s - \varepsilon_e \sin^2\,\theta}. \quad (4)$$

(2) For the case of a beam incident on the film from above (BB_+, see Fig. 1)

$$H_e = H_0 J_1(r\sqrt{\varepsilon_s}\,\sin\,\theta) T_+ e^{-i\chi_e z}, \quad (z \le 0), \quad (5)$$

$$H_s = H_0 J_1(r\sqrt{\varepsilon_s}\,\sin\,\theta)[e^{-i\chi_s(z-h)} + R_+ e^{i\chi_s(z-h)}], \quad (z \geq h),$$

$$R_+ = \frac{\Lambda_{sf} - \Lambda_{ef}E^2}{1 - \Lambda_{ef}\Lambda_{sf}E^2}, \quad T_+ = \frac{(1-\Lambda_{ef})(1+\Lambda_{sf})E}{(1-\Lambda_{ef}\Lambda_{sf}E^2)}. \tag{6}$$

and in this case the axial components of wave vectors are

$$\chi_e = \sqrt{\varepsilon_e - \varepsilon_s \sin^2\,\theta}, \quad \chi_f = \sqrt{\varepsilon_f - \varepsilon_s \sin^2\,\theta}, \quad \chi_s = \sqrt{\varepsilon_s}\cos\,\theta. \tag{7}$$

H_0 is the amplitude of the magnetic field in the illuminating laser beam and θ is the angle of the Bessel beam relative to positive or negative vectors normal to the film surface. We use in our formulas subscripts e, f, and s, designating the domains of the environment, film and support, respectively.

The formulas for the components of the electric field follow from the Maxwell equations:

$$E_r = -\frac{i}{\varepsilon r}\frac{\partial(rH_\varphi)}{\partial z}, \quad E_z = \frac{i}{\varepsilon r}\frac{\partial(rH_\varphi)}{\partial r}. \tag{8}$$

In the case of attenuated total reflection (ATR): $\theta > \theta_{cr} = \arcsin(\sqrt{\frac{\varepsilon_e}{\varepsilon_s}})$, and in the domain $z \leq 0$ there is a nonpropagating (evanescent) EM field. The axial and radial components of the electric field are

$$E_z = iE_0 T_+ \sqrt{\frac{\varepsilon_s}{\varepsilon_e}}\sin\,\theta J_0(r\sqrt{\varepsilon_s}\,\sin\,\theta)e^{-|\chi_e z|}, \tag{9}$$

$$E_r = -iE_0 T_+ \frac{\chi_e}{\sqrt{\varepsilon_e}} J_1(r\sqrt{\varepsilon_s}\,\sin\,\theta)e^{-|\chi_e z|}, \tag{10}$$

where $E_0 = H_0/\sqrt{\varepsilon_e}$ is the amplitude of electric field in the incident EM wave.

The dimensionless amplification factor for the electric field on the film surface at the point $r=0$, $z=-d$ is introduced as a ratio $A = |E_z/E_0|$. From formula (9) and a similar expression derived from formula (1) follow the film amplification factors, when BB illuminates the film from above (+) or from below (−), respectively

$$A_+ = |e^{i\chi_e d}T_+|\sqrt{\frac{\varepsilon_s}{\varepsilon_e}}\,\sin\,\theta, \tag{11}$$

$$A_- = |e^{-i\chi_e d} + R_- e^{i\chi_e d}|\sin\,\theta. \tag{12}$$

One could build other external light sources that are closer to experimentally used illumination schemes: by multiplying fields expressed by formulas (1), (2), (5), and (6) with some weight function (apodization function[29]) depending on the angle of incidence and integrating over a certain angular range. Such a source also obeys Maxwell's equation. Here we intentionally stick to Bessel beams of a defined angle because the results will show clearly the correspondence between the field enhancement by illumination from one angle and dipole radiation into the same angle.

B. Dipole illumination of a thin metal film covering a dielectric support

The Hertz potential[37] for a dipole placed near a metal semispace was derived previously.[35] Here this approach is extended to the case when the dipole is placed near a dielectric support covered by a thin metal film.[36] The Hertz potential for a dipole placed below the film are described by formulas

$$\Pi_s = i\int_0^\infty T_- e^{i\chi_s(z-h)+i\chi_e d}J_0(\gamma r)\frac{\gamma d\gamma}{\chi_e}, \tag{13}$$

$$\Pi_e = i\int_0^\infty [e^{i\chi_e|z+d|} + R_- e^{i\chi_e|z-d|}]J_0(\gamma r)\frac{\gamma d\gamma}{\chi_e}, \tag{14}$$

where subscripts s and e indicate when observation point is situated in the dielectric support ($z>h$) or in empty space ($z<0$), respectively, d is the dipole/film distance (the dipole coordinate is $z_d = -d < 0$), the transmission and reflection coefficients are

$$T_- = \frac{(1+\Lambda_{ef})(1-\Lambda_{sf})E}{1-\Lambda_{ef}\Lambda_{sf}E^2}, \quad R_- = \frac{\Lambda_{ef} - \Lambda_{sf}E^2}{1-\Lambda_{ef}\Lambda_{sf}E^2}, \quad E = e^{i\chi_f h}, \tag{15}$$

$$\Lambda_{ef} = \frac{\chi_e\varepsilon_f - \chi_f\varepsilon_e}{\chi_e\varepsilon_f + \chi_f\varepsilon_e}, \quad \Lambda_{sf} = \frac{\chi_s\varepsilon_f - \chi_f\varepsilon_s}{\chi_s\varepsilon_f + \chi_f\varepsilon_s},$$
$$\chi_i = \sqrt{\varepsilon_i - \gamma^2}, \quad (i = e,f,s). \tag{16}$$

Formulas (13) and (14) were derived from the Helmholtz wave equation by Hankel integral transformation. They represent the Hertz potential as a superposition of cylindrical waves, which have in various regions the same radial components of wave vector γ and different axial wave vector's components χ_i. The Hertz potential determines the magnetic field: $H_\varphi = iH_*\frac{\partial\Pi}{\partial r}$, where $H_* = k^3 p_0$ is the characteristic magnetic field for the dipole, p_0 is the electric dipole moment, $k = \omega/c$ is the vacuum wave number for dipole radiation, and the electric field components are obtained via Maxwell's Eq. (8).

For the following calculation of the dipole-energy fluxes we need the fields:

$$E_r^{(s)} = \frac{H_*}{\varepsilon_s}\int_0^\infty \chi_s T_- J_1(\gamma r)e^{i\chi_s(z-h)+i\chi_e d}\frac{\gamma^2 d\gamma}{\chi_e}, \quad (z \geq h), \tag{17}$$

$$H_\varphi^{(s)} = H_*\int_0^\infty T_- J_1(\gamma r)e^{i\chi_s(z-h)+i\chi_e d}\frac{\gamma^2 d\gamma}{\chi_e}, \quad (z \geq h), \tag{18}$$

$$E_r^{(e)} = -\frac{H_*}{\varepsilon_e}\int_0^\infty [e^{i\chi_e|z+d|} + R_- e^{i\chi_e|z-d|}]J_1(\gamma r)\gamma^2 d\gamma, \quad (z \leq -d), \tag{19}$$

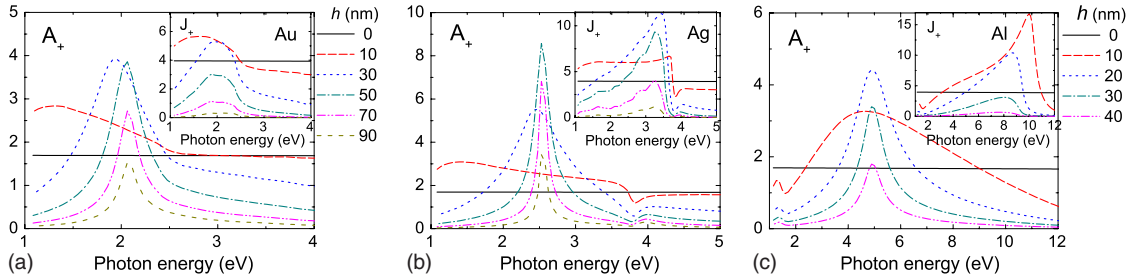

FIG. 2. (Color online) The field-enhancement factor A_+ and dipole radiation J_+ (in the insets) are shown for three metallic films: (a) gold (Ref. 39); (b) silver (Ref. 39); and (c) aluminum (Ref. 40). Curves correspond to different films thicknesses h.

$$H_\varphi^{(e)} = H_* \int_0^\infty [e^{i\chi_e|z+d|} + R_- e^{i\chi_e|z-d|}] J_1(\gamma r) \frac{\gamma^2 d\gamma}{\chi_e}, \quad (z \le -d). \tag{20}$$

By integration of the z component of the Poynting vector[35] $S_z = \frac{c}{8\pi}\mathrm{Re}\{E_r^* \times H_\varphi\}$ on the planes situated above the film ($z > h$) or below the dipole ($z < -d$) one can obtain the dipole-energy fluxes directed into the upper or lower semispaces

$$j_+ = \frac{ck^4 p_0^2}{4\varepsilon_s} \int_0^{\sqrt{\varepsilon_s}} \left| \frac{\chi_s}{\chi_e} e^{i\chi_e d} T_- \right|^2 \frac{\gamma^3 d\gamma}{\sqrt{\varepsilon_s - \gamma^2}},$$

$$j_- = \frac{ck^4 p_0^2}{4\varepsilon_e} \int_0^{\sqrt{\varepsilon_e}} |1 + R_- e^{2i\chi_e d}|^2 \frac{\gamma^3 d\gamma}{\sqrt{\varepsilon_e - \gamma^2}}.$$

Dividing values j_+ and j_- by the semiflux of energy of a free dipole

$$j_* = \frac{1}{2} \frac{ck^4 p_0^2}{3} \sqrt{\varepsilon_e}, \tag{21}$$

and by introducing a new variable of integration τ and by substituting of $\gamma^2 = \varepsilon_s(1-\tau^2)$ in j_+ and $\gamma^2 = \varepsilon_e(1-\tau^2)$ in j_-, two dimensionless expressions for dipole-energy fluxes are obtained

$$J_+ = \frac{3}{2} \sqrt{\frac{\varepsilon_s}{\varepsilon_e}} \int_0^1 \left| \frac{\chi_s}{\chi_e} e^{i\chi_e d} T_- \right|^2 (1-\tau^2) d\tau, \tag{22}$$

$$J_- = \frac{3}{2} \int_0^1 |1 + R_- e^{2i\chi_e d}|^2 (1-\tau^2) d\tau. \tag{23}$$

These values are the enhancement factors of dipole radiation caused by the metallic film only (in the absence of a nanoparticle). The formula (23) gives for thick film the Sommerfeld's[38] result for the radiation of a dipole placed close to semispace with finite conductivity.

C. Influence of film thickness and illumination angle on the field-enhancement factor A, the dipole flux J, and the film-enhancement factor I

Illumination of a film at angles θ larger than the critical angle of total reflection θ_{cr} ($\theta_{cr} = 41.81°$ for glass/air interface) serves as effective method of exciting plasmons in the metallic film (Kretschman, Ref. 28). Let us fix the film/dipole distance d ($d = 0.5$ nm) and illumination angle ($\theta = 45°$) and consider the influence of film thickness h on the factors A_+ and J_+. The plasmon resonances can be recognized in the values A_+ and J_+, shown in Fig. 2 for the three metals, gold, silver, and aluminum, as a function of the photon energy $\hbar\omega$ (in electron volt, eV) instead of the wavelength. It helps to show clearly details in the short-wavelength region. As for a thickness $h = 50$ nm for silver and gold and $h = 20$ nm for aluminum the resonant plasmon maximum in the factor A_+ is the highest, these optimal values are chosen in our calculations below. Note, that the highest maximum for the dipole factor J_+ (shown in the insets) occurs for thinner films: $h = 30$ nm (silver, gold) and 10 nm (aluminum). From Fig. 2 one can conclude that in the case of ATR the amplified electric field A_+ for some resonant wavelength and for optimal film thickness is enhanced by a factor of 8–10 times in Ag films and 4–5 in Al and Au films, respectively. Note, that for aluminum films the dipole factors J_+ are not enhanced in the visible but are strongly enhanced in the ultraviolet region.

In Fig. 3 the factors A_+ and A_- (in the insets) are shown for film thicknesses 50 nm (Ag, Au) and 20 nm (Al), and beam angles $\theta = 41°$, 42°, 43°, 44°, and 45°, respectively. The first angle is smaller than the critical angle of total reflection ($\theta_{cr} = 41.81°$), and the dramatic difference between ATR and non-ATR ($\theta = 41°$) regimes of film illumination is clearly seen in factors A_+. For ATR configuration the plasmonic resonances in A_+ spectra are present. Factor A_- corresponds to illumination coming from below (BB_). It has no plasmonic resonances and its dependence on the illumination angle is weak.

For relatively "thick" films ($h > 40$ nm for Ag and Au films and $h > 15$ nm for Al films) one can derive an approximate formula for a beam angle at which the factor A_+ has a maximum

$$\theta_{\max} = \sin^{-1}\left[\mathrm{Re}\left(\frac{\varepsilon_s}{\varepsilon_e} + \frac{\varepsilon_s}{\varepsilon_f(\omega)} \right)^{-1/2} \right]. \tag{24}$$

This formula follows from the denominator $(\chi_e\varepsilon_f + \chi_f\varepsilon_e)$ in the factor $(1 - \Lambda_{ef})$, which is contained in the transmission coefficient T_+ [see Eqs. (5)–(7)]. By putting it to zero a complex expression $\sin\theta_{\max} = [(\varepsilon_s/\varepsilon_e) + \varepsilon_s/\varepsilon_f(\omega)]^{-1/2}$ can be obtained, the real part of which gives expression (24). For small light frequencies ω the value $|\varepsilon_f|$ is much larger than

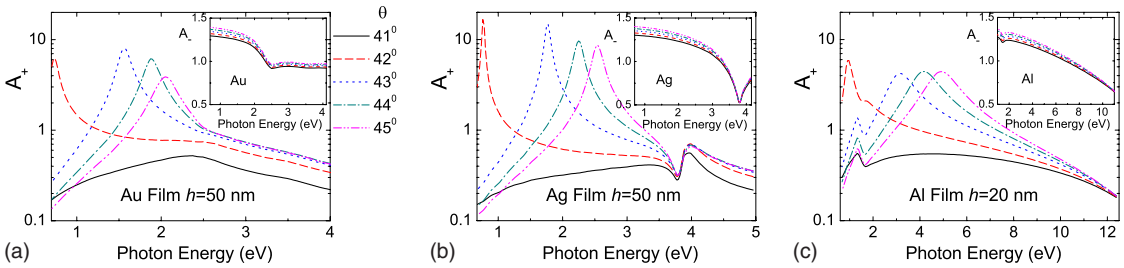

FIG. 3. (Color online) The factors A_+ and A_- (insets) for metallic films made of: (a) gold, (b) silver, and (c) aluminum. Curves correspond to different BB angles θ.

the dielectric permittivity ε_s and the angle $\theta_{\max}$ approaches the critical angle.

When a nanoparticle is retracted away to infinity, the illumination field (A) and the dipole radiation (J) are enhanced only due to the presence of metallic film. We will consider four film-enhancement factors: two for the enhanced electric field at the dipole position for a beam coming from above (A_+) *or* from below (A_-) and two factors for the enhanced dipole radiation into the upper (J_+) *and* lower (J_-) semispaces. By using words "or" and "and" we will underline that illumination beams are applied alternatively (BB_+ *or* BB_-) and the fluxes J_+ *and* J_- are the spatially separate but simultaneous parts of the total dipole radiation. The total film-enhancement factor is $I=A^2J$. Due to the independence of A and J there are four combinations

$$I_{++}=A_+^2J_+, \quad I_{+-}=A_+^2J_-, \quad I_{-+}=A_-^2J_+, \quad I_{--}=A_-^2J_-. \tag{25}$$

In Fig. 4 these values are shown for the chosen film thicknesses, at BB angle 45°, and for a surface/dipole distance $d=0.5$ nm. In the insets of Fig. 4 one can see the optical constants n, $\kappa(\sqrt{\varepsilon}=n+i\kappa)$ for the metals used in our calculations according to Johnson and Christy[39] for silver and gold and according to Palik[40] for aluminum. Note, that the optical constants have no resonances in the wavelength domain, where the plasmonic peaks are situated.

An interesting feature is seen in Fig. 3: by a small change in angle for $\theta>\theta_{cr}$ the maximum in A_+ can scan the whole spectral region from IR to UV. The largest maximum in value I_{++} is for Ag film at $\theta=44°$ [Fig. 4(b)]: $I_{++}\approx 300$. The radial size of the central spot in the BB giving rise to the field enhancement A_+ can be estimated from the first root of the Bessel function $J_0(\cdot)$: $r_*=2.2\lambda/\sin\theta$ corresponding to a spot size comparable to the wavelength. This nonlocal diffraction limited central spot will create a strong background signal to the local-field enhancement by the nanoparticle. In order to eliminate this nonlocal enhancement effect we will introduce below relative enhancement factors F and D.

III. METHOD OF CALCULATION

A. Green's function and BIEs

For problems of axial symmetry a modified Green's function should be used. It can be obtained by multiplying the three-dimensional (3D) Green's function for free space with $\cos\varphi$ and integration on the azimuth angle φ:[41]

$$G_{in}=\int_0^{2\pi}\frac{e^{i\sqrt{\varepsilon_p}|\vec{r}-\vec{\rho}|}}{4\pi|\vec{r}-\vec{\rho}|}\cos\varphi\ d\varphi, \tag{26}$$

where $|\vec{r}-\vec{\rho}|=\sqrt{r^2+\rho^2-2r\rho\cos\varphi+(z-\zeta)^2}$, ρ and ζ are the integration coordinates, and r and z are the observation coordinates. This function is used for the solution of the inner Maxwell problem, and therefore the permittivity in Eq. (26) is ε_p, the particle's permittivity. For the field $H_\varphi^{(p)}$ inside the particle the solution is represented by the Green's formula

$$-H_\varphi^{(p)}(O)=\int_\Gamma\left[H_\varphi^{(p)}(\Gamma)\frac{\partial G_{in}(O,\Gamma)}{\partial\nu}-G_{in}(O,\Gamma)\frac{\partial H_\varphi^{(p)}(\Gamma)}{\partial\nu}\right]\rho d\Gamma, \tag{27}$$

where the observation point is designated by letter O (coordinates r and z) and the integration points (ρ, ζ), placed on

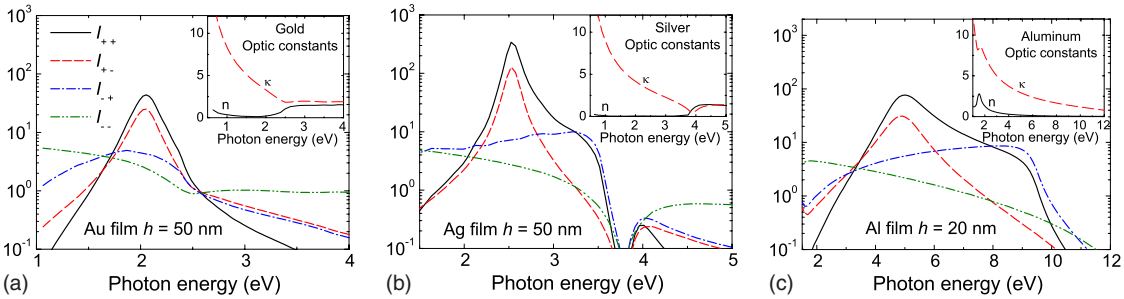

FIG. 4. (Color online) The film-enhancement factors $I=A^2J$ for BB angle $\theta=45°$ and three metals: (a) gold, (b) silver, and (c) aluminum. In the insets the optic constants of corresponding metals are shown. The optimal film thicknesses, indicated in figures, are used.

the particle's surface, are noted by letter Γ. An external normal to the particle surface is designated by the letter ν. Integration is performed along the meridian line going from one pole to another pole of the particle (contour Γ in Fig. 1).

In order to build the Green's function describing the outer solution for the domain outside the particle we should consider the equation for it

$$\frac{1}{r}\frac{\partial}{\partial r}r\frac{\partial}{\partial r}G_i + \frac{\partial^2 G_i}{\partial z^2} - \frac{1}{r^2}G_i + \varepsilon_i G_i = -\frac{\delta(r-\rho)}{r}\delta(z-\zeta), \tag{28}$$

where subscript i designates letters e, f, and s for three space domains with different permittivities: the empty subspace (under the film), the metallic film, and the dielectric support (semispace above the film), respectively.

Boundary conditions, expressing the continuity of tangential EM-field components, on the film surfaces are

$$z=0: \quad G_e = G_f, \quad \frac{1}{\varepsilon_e}\frac{\partial G_e}{\partial z} = \frac{1}{\varepsilon_f}\frac{\partial G_f}{\partial z}, \tag{29a}$$

$$z=h: \quad G_s = G_f, \quad \frac{1}{\varepsilon_s}\frac{\partial G_s}{\partial z} = \frac{1}{\varepsilon_f}\frac{\partial G_f}{\partial z}. \tag{29b}$$

It was obtained for $\zeta \le 0$

$$G_e = i\int_0^\infty [e^{i\chi_e|z-\zeta|} + R\_e^{i\chi_e|z+\zeta|}]\frac{J_1(\gamma r)J_1(\gamma\rho)\gamma d\gamma}{2\chi_e}, \quad (z \le 0), \tag{30}$$

$$G_s = i\int_0^\infty T\_e^{-i\chi_e\zeta + i\chi_s(z-h)}\frac{J_1(\gamma r)J_1(\gamma\rho)\gamma d\gamma}{2\chi_e}, \quad (z \ge h). \tag{31}$$

Now the scattered magnetic field H'_φ in the regions below and above the film is represented through the Green's formula

$$H'_\varphi(X) = \int_\Gamma \left[H'_\varphi(\Gamma)\frac{\partial G_{out}(X,\Gamma)}{\partial \nu} - G_{out}(X,\Gamma)\frac{\partial H'_\varphi(\Gamma)}{\partial \nu}\right]\rho d\Gamma \tag{32}$$

with G_{out} expressed by formulas (30) and (31), respectively. The field H'_φ in the last formula is the scattered field outside the particle. The external points (relative to the particle volume) are designated by letter X and the integration points are designated again by letter Γ.

The boundary conditions for fields and normal derivatives on the particle surface are

$$H_\varphi^{(p)} = H'_\varphi + H_\varphi^{(0)},$$

$$\frac{1}{\varepsilon_p}\frac{\partial H_\varphi^{(p)}}{\partial \nu} = \frac{1}{\varepsilon_e}\frac{\partial (H'_\varphi + H_\varphi^{(0)})}{\partial \nu}, \tag{33}$$

where the outer source field $H_\varphi^{(0)}$ is introduced. This field is described above. It is: (1) the field produced by the Bessel beam when the field-enhancement factor is calculated or (2) the dipole field when the dipole-enhancement factor (DEF) is calculated. Note that the sum of scattered and incident fields $H_\varphi = H'_\varphi + H_\varphi^{(0)}$ is the full magnetic field outside the nanoparticle.

From the Green's formulas (27) and (32) and boundary conditions Eq. (33) the next system of BIEs can be derived for two unknown values H'_φ and $\frac{\partial H'_\varphi}{\partial \nu}$ on Γ

$$-\alpha(H'_\varphi + H_\varphi^{(0)}) = \int_\Gamma \left[(H'_\varphi + H_\varphi^{(0)})\frac{\partial G_{in}}{\partial \nu} - \frac{\varepsilon_p}{\varepsilon_e}G_{in}\frac{\partial (H'_\varphi + H_\varphi^{(0)})}{\partial \nu}\right]\rho d\Gamma, \tag{34}$$

$$\alpha H'_\varphi = \int_\Gamma \left[H'_\varphi \frac{\partial G_{out}}{\partial \nu} - G_{out}\frac{\partial H'_\varphi}{\partial \nu}\right]\rho d\Gamma, \tag{35}$$

where $\alpha = 0.5$.

Note that the illumination field $H_\varphi^{(0)}$ is also an exact solution of the Maxwell equation. From this fact follows an identity for $H_\varphi^{(0)}$, which is very useful for the control of accuracy of the calculated Green's function G_{out} and the field $H_\varphi^{(0)}$

$$-\alpha H_\varphi^{(0)} = \int_\Gamma \left[H_\varphi^{(0)}\frac{\partial G_{out}}{\partial \nu} - G_{out}\frac{\partial H_\varphi^{(0)}}{\partial \nu}\right]\rho d\Gamma. \tag{36}$$

For example, the absolute value of the difference between the left and right sides of Eq. (36) in our calculations for one hundred control points on the contour of a nanoparticle was less than 10^{-4} for small nanobodies (50–200 nm) and about 10^{-2} for long nanoparticles (1–5 μm).

We add the BIE Eq. (36) to the Eq. (35), introduce the full field H_φ and its normal derivative $\frac{\partial H_\varphi}{\partial \nu}$ as the main wanted values, and obtain for them the final system of BIEs

$$\alpha H_\varphi + \int_\Gamma \left[H_\varphi \frac{\partial G_{in}}{\partial \nu} - \frac{\varepsilon_p}{\varepsilon_e}G_{in}\frac{\partial H_\varphi}{\partial \nu}\right]\rho d\Gamma = 0, \tag{37}$$

$$\alpha H_\varphi - \int_\Gamma \left[H_\varphi \frac{\partial G_{out}}{\partial \nu} - G_{out}\frac{\partial H_\varphi}{\partial \nu}\right]\rho d\Gamma = H_\varphi^{(0)}. \tag{38}$$

The solutions of the system of BIEs permit to represent the outer and inner fields via the formulas (27) and (32).

B. FEF

Let us introduce a measure of the field enhancement caused by the NP at the dipole position, the field-enhancement factor

$$\mathrm{FEF} = \left| \frac{E_z(r=0; z=-d)}{E_0} \right|, \tag{39}$$

where E_0 is the amplitude of the electric field in the incident laser beam, E_z is the axial component of electric field. Obviously, the maximal electric field is expected at the pole of the nanoparticle which is placed close to the film surface. At the other pole placed far from the film surface the electric field is also interesting to see. It illustrates modes excited in the

nanoparticle. This dimensionless field will be indicated as $\mathrm{FEF}_{\mathrm{far}}$ below.

C. Dimensionless dipole-energy flux or DEF

By combining fields of the dipole and nanoparticle and by substituting them into the Pointing vector and integrating of the z component of the vector S_z over the control planes we obtain two total dipole-energy fluxes directed up and down relative to the film. Let's introduce dimensionless ratios by relating these fluxes to the semiflux of the free dipole [j_* described by formula (21)] to obtain the dimensionless dipole-enhancement factors or dipole-energy fluxes

$$\mathrm{DEF}_+ = \frac{3}{2}\sqrt{\frac{\varepsilon_s}{\varepsilon_e}}\int_0^1 \left|\frac{\chi_s}{\chi_e}\Phi T_-\right|^2 (1-\tau^2)d\tau, \tag{40}$$

$$\mathrm{DEF}_- = \frac{3}{2}\int_0^1 |\Psi|^2 (1-\tau^2)d\tau, \tag{41}$$

where

$$\Phi = e^{i\chi_e d} - \frac{1}{2i}\int_\Gamma \left\{ H'_\varphi \left\{ \nu_\rho \left[J_0(\eta) - \frac{J_1(\eta)}{\eta} \right] - i\nu_\zeta \chi_e \rho \frac{J_1(\eta)}{\eta} \right\} - \rho \frac{J_1(\eta)}{\eta}\frac{\partial H'_\varphi}{\partial \nu} \right\} e^{-i\chi_e \zeta} \rho d\Gamma, \tag{42}$$

$$\Psi = F_d - \frac{1}{2i}\int_\Gamma \left\{ H'_\varphi \left\{ \nu_\rho F_+ \left[J_0(\eta) - \frac{J_1(\eta)}{\eta} \right] - i\nu_\zeta \chi_e \rho F_- \frac{J_1(\eta)}{\eta} - \rho F_+ \frac{J_1(\eta)}{\eta}\frac{\partial H'_\varphi}{\partial \nu} \right\} \right\} \rho d\Gamma, \tag{43}$$

where $\eta = \rho \cdot \gamma(\tau)$, $F_\pm = \pm e^{i\chi_e \zeta} + R_- e^{-i\chi_e \zeta}$, $F_d = e^{-i\chi_e d} + R_- e^{i\chi_e d}$, and ν_ρ and ν_ζ are the components of the external normal and values R_-, T_-, χ_e, χ_s, and $\gamma(\tau)$ are the same as described for a dipole in formulas (15), (16), (22), and (23).

Note that the values H'_φ, and $\frac{H'_\varphi}{\partial \nu}$, staying under the integrals in the formulas (42) and (43), are the dimensionless solutions of the system of BIEs [Eqs. (34) and (35)] with the dipole source illumination described above. Dimensionless dipole-energy fluxes, DEF_+ and DEF_-, represent a full enhancement of the dipole radiation caused by metallic film and nanoparticle.

D. Angular distribution of the dipole radiation

One can arrive by another way to the formulas (40) and (41) for the flux of dipole energy. The asymptotic value of the Green's function in the far zone for large z and r is represented by the expression

$$G = \frac{w(\zeta,\rho)}{R} e^{i\sqrt{\varepsilon}R},$$

$$R = \sqrt{r^2 + z^2}, \tag{44}$$

where ε is the medium permittivity, R is the radius in spherical system of coordinates, and w is a spherical wave amplitude. The wave amplitude w in the upper semispace is

$$w_s = \frac{\chi_s}{2\chi_e} T_- e^{-i\chi_e \zeta - i\chi_s h} J_1(\gamma_s \rho), \tag{45}$$

where $\gamma_s = \sqrt{\varepsilon_s}\sin\theta$, $\chi_s = \sqrt{\varepsilon_s}\cos\theta$, and $\chi_e = \sqrt{\varepsilon_e - \varepsilon_s \sin^2\theta}$.

In the lower semispace the amplitude w is represented by expression

$$w_e = \frac{1}{2}(e^{i\chi_e \zeta} + R_- e^{-i\chi_e \zeta}) J_1(\gamma_e \rho), \tag{46}$$

where $\gamma_e = \sqrt{\varepsilon_e}\sin\theta$, $\chi_e = \sqrt{\varepsilon_e}\cos\theta$, $\chi_s = \sqrt{\varepsilon_s - \varepsilon_e \sin^2\theta}$, and θ is the azimuth angle in spherical coordinates (counted from the positive or negative z semiaxes, respectively). Formulas (44)–(46) are obtained from expressions (30) and (31) by the saddle-point approximation method. For the case without NP (considering only the point dipole) our results coincide with formulas from the paper of Sakoda *et al.*[42]

The full magnetic and electric fields H_φ and E_ϑ, calculated from the superposition of incident and scattered dipole fields and inserted in the time-averaged radial component of the Pointing vector, give the energy-flux density

$$S_R = \frac{c}{8\pi} E_\vartheta H^*_\varphi. \tag{47}$$

By using a dipole characteristic field $H_* = k^3 p_0$ (p_0 is the dipole moment) and the dipole-energy semiflux j_* [see formula (21)], we obtain the dimensionless angular distribution functions

$$P(\theta) = \frac{2\pi R^2 S_R(\theta)}{j_*}$$

for the dipole radiation in the upper and lower semispaces

$$P_+(\theta) = \frac{3}{2}\sin^2\theta \sqrt{\frac{\varepsilon_s}{\varepsilon_e}} \left| \frac{\chi_s}{\chi_e} T_- \right| \left| e^{i\chi_e d} - \frac{1}{2i}\int_\Gamma \left\{ H'_\varphi \left\{ \nu_\rho \left[J_0(\eta) - \frac{J_1(\eta)}{\eta} \right] - i\nu_\zeta \chi_e \rho \frac{J_1(\eta)}{\eta} \right\} - \rho \frac{J_1(\eta)}{\eta}\frac{\partial H'_\varphi}{\partial \nu} \right\} e^{-i\chi_e \zeta} \rho\, \partial\Gamma \right|^2, \tag{48}$$

$$P_-(\theta) = \frac{3}{2}\sin^2\theta \left| F_d - \frac{1}{2i}\int_\Gamma \left\{ H'_\varphi \left\{ \nu_\rho F_+ \left[J_0(\eta) - \frac{J_1(\eta)}{\eta} \right] - i\nu_\zeta \chi_e \rho F_- \frac{J_1(\eta)}{\eta} - \rho F_+ \frac{J_1(\eta)}{\eta}\frac{\partial H'_\varphi}{\partial \nu} \right\} \right\} \rho\, \partial\Gamma \right|^2, \tag{49}$$

where

$$F_d = e^{-i\chi_e d} + R_- e^{i\chi_e d}, \quad F_\pm = \pm e^{i\chi_e \zeta} + R_- e^{-i\chi_e \zeta},$$

$$R_- = \frac{\Lambda_{ef} - \Lambda_{sf} E^2}{1 - \Lambda_{ef}\Lambda_{sf} E^2}, \quad T_- = \frac{(1+\Lambda_{ef})(1-\Lambda_{sf})E}{(1 - \Lambda_{ef}\Lambda_{sf} E^2)},$$

$$E = \exp(i\chi_f h),$$

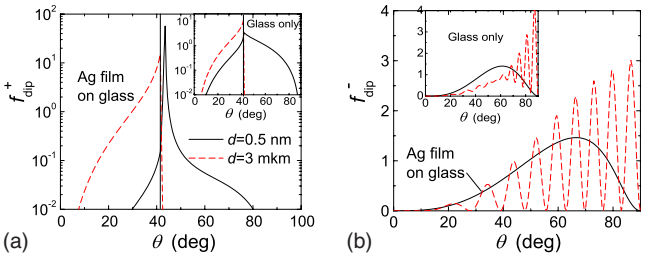

FIG. 5. (Color online) Angular distribution functions of dipole radiation for Ag film (without NP) at a photon energy of 1.97 eV (λ=630 nm). Film thickness is h=50 nm and in the insets the variants for glass only (with h=0) are shown.

$$\Lambda_{ef} = \frac{\chi_e \varepsilon_f - \chi_f \varepsilon_e}{\chi_e \varepsilon_f + \chi_f \varepsilon_e}, \quad \Lambda_{sf} = \frac{\chi_s \varepsilon_f - \chi_f \varepsilon_s}{\chi_s \varepsilon_f + \chi_f \varepsilon_s},$$

$$\chi_i = \sqrt{\varepsilon_i - \gamma^2}, \quad (i = e,f,s,),$$

$$\gamma = \sqrt{\varepsilon_j} \sin\theta, \quad (j = e,s).$$

By integration of expression (48) and (49) over the full angular range of the upper and lower semispaces we obtain again the formulas (40) and (41) for dipole radiation into the dielectric support and into the lower subspace, respectively

$$\mathrm{DEF}_+ = \int_0^{\pi/2} P_+(\theta) \sin\theta \, d\theta,$$

$$\mathrm{DEF}_- = \int_0^{\pi/2} P_-(\theta) \sin\theta \, d\theta.$$

In the case when the NP is retracted to infinity and the integral's inputs in formulas (48) and (49) disappear one can note an important feature: due to a simple connection between the transmission coefficients T_+ and T_-,

$$T_+ = \frac{\varepsilon_e}{\varepsilon_s} \frac{\chi_s}{\chi_e} T_-,$$

the angle distribution functions are exactly proportional to the illumination intensity at the dipole position: $P_+(\theta) \propto A_+^2(\theta)$ and $P_-(\theta) \propto A_-^2(\theta)$. This is a consequence of the known reciprocity theorem in optics[43] and it was used by Le Ru and Etchegoin[44] for proving the proportionality of a SERS signal to the fourth power of the local electric field.

Let us introduce two normalized angular distribution functions for the cases when the NP is present or absent

$$f_{\mathrm{NP}}^{+/-}(\theta) = P_{+/-}(\theta)/\mathrm{DEF}_{+/-},$$

$$f_{dip}^{+/-}(\theta) = \lim_{g \to \infty} \{ f_{\mathrm{NP}}^{+/-}(\theta) \}. \tag{50}$$

In the case when the NP is retracted to infinity the angular distribution functions $f_{dip}^{+/-}(\theta)$ are shown in Figs. 5(a) and 5(b) for a photon energy of 1.97 eV or a wavelength of 630 nm, for Ag film thickness h=0 and 50 nm, and for two surface/dipole distances d=0.5 and 3000 nm. The function shown in Fig. 5(a) has a very narrow peak situated at $\theta_{\max}$=43.34°. This value corresponds exactly to the position of the maximum of A_+ at the wavelength of 630 nm as obtained by formula (24). One can see that the dipole placed close to the film (d=0.5 nm) radiates strongly into the forbidden sector $\theta > \theta_{cr}$, and the distant dipole (d=3 μm) sends a very small amount of radiation into this sector. The light transmitted into the forbidden sector, according to expression (48), and the film-enhancement factor A_+, determined by formula (11), contain the same factor $|e^{i\chi_e d}|^2$, which describes the exponential decay versus the surface/dipole distance d. These interesting features of radiation of a dipole situated in the near or far zones of a dielectric surface were described previously by Lukosz and Kunz[45] and in the book of Novotny and Hecht.[46]

E. Boundary element method

The system of BIEs [Eqs. (37) and (38)] may be effectively resolved by the boundary element method (BEM).[33–36,41] BEM works especially well for problems described by Laplace and Helmholtz equations with piece-wise constant material properties. This is exactly the problem what we have. BEM was widely used in radio technique calculations, in microwave and antenna theory. In the last decade similar methods, called surface integral equation methods, are also used in nano-optics[47–50] for 3D calculations. These methods have advantages in comparison to others: (1) they permit to reduce the dimension of the problem and to decrease a total number of unknown values; (2) the surface can be divided in a much more flexible way into small cells and the density of the nodes can be increased in points of high field intensity (hot spots). Our method differs from the others by taking into account the effects of a layered medium. For this we pay a long time to calculate so-called Sommerfeld integrals,[38] which determine the Green's function. Additional reduction in the dimension of the problem due to the axial symmetry leads us to a system of one-dimensional integral equations and permits to investigate many cases in a rich space of parameters of the problem.

When the integration point approaches the observation point (both on contour Γ) the Green's function and its derivative have a singular behavior. Zakharov and Eremin[41] showed that singularities in G and $\frac{\partial G}{\partial n}$ have a logarithmic character and may be subtracted and integrated during calculation of integrals along the elements. For the calculation of the nonsingular part of the Green's function and its normal derivative an adoptive algorithm QUANC8 (Ref. 51) was used. Calculations of integrals of the Green's function and its normal derivative along the boundary element are performed by using a six-point Gauss formula. By applying a modified Gauss algorithm[51] the logarithmic singularities mentioned above are also successfully integrated.

IV. INFLUENCE OF A NANOPARTICLE ON A RAMAN SIGNAL

The calculations are performed for three metals: silver, gold, and aluminum, often used in near-field optic experiments. The nanoparticle and film are assumed to be made of the same metals. Due to a high conductivity in the visible and infrared, silver is the best metal for the field enhance-

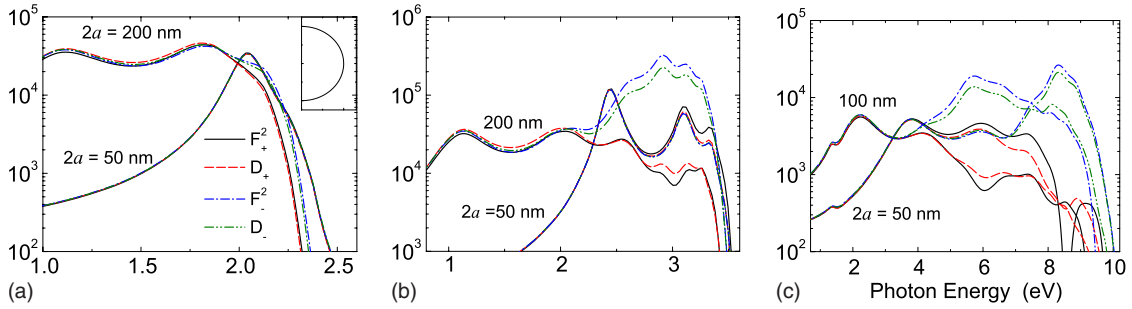

FIG. 6. (Color online) Relative enhancement factors F^2 and D for metallic spheres [(a) gold, (b) silver, and (c) aluminum] in dependence of the photon energy. In figure (a) all lines collapse to a single line for $2a=50$ nm. The same holds for figures (b) and (c) in the low-energy region for the dipolar peaks.

ment, although it is not so stable as gold. An interesting metal is aluminum, which has a high plasmonic activity in ultraviolet. In the following Secs. IV A–IV G the optimal film thickness is chosen, $h=50$ nm for Au and Ag and $h=20$ nm for Al films, the gap is $g=1$ nm (except in Sec. IV C), and the angle of the BB is $\theta=45°$ (except Secs. IV D, IV F, and IV G). In the insets of figures of this chapter the NP contour and size (in nm) are shown.

A. Definition of enhancement factors: *F*, *D*, REF

In order to investigate an influence of the nanoparticle we introduce the relative enhancement factors F and D determined by formulas

$$F_+ = \mathrm{FEF}_+/A_+, \quad F_- = \mathrm{FEF}_-/A_-, \tag{51}$$

$$D_+ = \mathrm{DEF}_+/J_+, \quad D_- = \mathrm{DEF}_-/J_-. \tag{52}$$

These factors permit to account for the direct impact of the NP on the enhancement of the local field and dipole radiation.

Let us introduce the total enhancement factor for Raman radiation as a product of two enhancement factors FEF^2 and DEF introduced earlier

$$\mathrm{REF} = \mathrm{FEF}^2(\omega)\mathrm{DEF}(\omega - \omega_{mol}). \tag{53}$$

For simplicity we will ignore the shift produced by the molecule frequency ω_{mol} and will take DEF also at the same frequency of the incoming laser light ω. By introducing the film-enhancement factor $I=A^2J$ we can rewrite this formula as $\mathrm{REF}=IF^2D$. There are four REF factors for the four cases described above by formulas (25) for the factors I

$$\mathrm{REF}_{++} = I_{++}F_+^2D_+, \quad \mathrm{REF}_{+-} = I_{+-}F_+^2D_-,$$
$$\mathrm{REF}_{-+} = I_{-+}F_-^2D_+, \quad \mathrm{REF}_{--} = I_{--}F_-^2D_-. \tag{54}$$

It should be mentioned that REF is not the most relevant enhancement factor for Raman radiation because REF includes I, focusing of the light beam to a diffraction-limited spot, which causes a large background for the very local near field of the nanoparticle. We remind that the I factors have a complex dependence on light frequency and on parameters θ, d, and h (see Figs. 2–4) and via the value I this dependence is included into the REF factors. We will not use factor REF. The most relevant enhancement factor is F^2D, and we will focus our attention on the components F^2 and D.

B. Influence of metal property and diameter of a spherical NP on the enhancement factors

The simplest shape of a NP is a sphere. We assume in this paragraph the fixed parameters: $\theta=45°$, $g=1$ nm, $d=g/2$, and a glass support of refractive index $n=1.5$. In Fig. 6 for three metallic spheres and films made of Au, Ag, and Al [figures (a), (b), and (c), respectively] the enhancement factors F^2 and D are shown. The film thickness h is 50 nm for figures (a) and (b) and 20 nm for (c). Spheres of two diameters are considered: for figures (a) and (b) $2a=50$ and 200 nm and for (c) $2a=50$ and 100 nm. In the last case the larger diameter is taken to be 100 nm because for the diameter 200 nm too many excited resonances would complicate the figure.

From Fig. 6 one can conclude: (1) there is a full coincidence of all introduced relative factors for the first (dipolar) resonance situated at low frequency; (2) enhancement factors exhibit two groups of close values (F_+^2, D_+) and (F_-^2, D_-) and a second group is larger than the first one; (3) the larger is the sphere diameter, the smaller is the photon energy, where the splitting into two groups occurs; and (4) the combined factor F^2D for aluminum and gold can reach 10^8 and for silver it can be more than 10^{10} (at appropriate sphere size and wavelength of light).

Why are the factors with plus subscripts smaller than the ones with minus subscripts? One can see from Fig. 6 that the factor's splitting occurs when the sphere radius becomes larger than the reduced wavelength ($a>\lambda$). For the chosen angle we have for BB_+ the ATR configuration: in the lower semispace there is an evanescent EM wave. Only the surface elements of the NP which are situated in the near zone ($z<2\lambda$) are strongly illuminated and can contribute to enhancement factor F_+^2. An exponentially decaying factor [$e^{-|\chi_e\xi|}$, formulas (5), (7), and (42)] decreases the contribution of distant parts of the NP to the enhanced field at the dipole position (F_+) and similarly diminishes the NP radiation into the "forbidden" ($\theta>\theta_{cr}$) angular sector above the film (D_+). In values F_-^2 and D_- such a damping factor is absent and the radiation from distant and near parts of the NP can interfere constructively and produce an additional enhancement as we

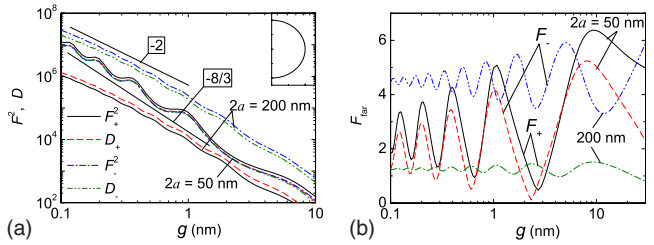

FIG. 7. (Color online) Enhancement factors vs g (gap) for Ag spheres of two diameters 50 and 200 nm at a photon energy of 3.1 eV ($\lambda=400$ nm): (a) relative factors at the sphere's close pole; (b) factor $F_{\text{far}}=E_z(z_2)/A$, at the sphere's pole situated far from the Ag film. The beam angle is $\theta=45°$.

see in Fig. 6. But this interference is not always constructive as will be demonstrated below.

C. Plasmonic gap modes

In Fig. 7(a) for two silver spheres with diameters $2a=50$ and 200 nm the factors F^2 and D are shown as a function of the film/particle gap distance g (the silver film thickness is $h=50$ nm). The dipole is placed in the center of a gap ($d=g/2$). In Fig. 7(b) the calculated normalized electric fields at the far sphere pole (F_{far}) are depicted. The factors F_{far} demonstrate clear "gap modes" especially well pronounced for a small sphere. The presence of intensive oscillations at the far pole of the nanobody demonstrates the global character of these modes: they depend strongly on the gap distance, but they are spreading over the whole volume of the nanobody. One can see a series of maxima (resonances) which occur at certain gaps g_m. The gap modes were discussed by elastic and inelastic light scattering.[52–55] Similar gap modes were described in calculations of light scattering by coupled metallic nanorods[48] and for a system of a nanosphere and a metallic sample.[34] It should be noted that by increasing the gap g these modes have to transform continuously into the known Mie modes of a single metallic sphere (not shown here). For very small gaps g, due to a strong interaction between charges on sphere and the counter charges induced on the film surface, these modes deviate dramatically from the Mie modes. The negative slopes -2 and $-8/3$ indicated in Fig. 7(a) correspond to slopes -1 and $-4/3$ for the field factor F. The first slope -2, seen for the large sphere, can be explained on the basis of an electrostatic analogy: the field in the gap is similar to the field in a parallel plate capacitor.[34] The average slope $-8/3$ for the field factor F^2, found for small spheres, has no clear explanation. But it is obviously an impact of the high amplitude of the gap modes, excited in the small sphere. One should mention that for gap distances smaller than 0.5 nm additional strong effects arise connected with atomic roughness, tunneling current, and Landau damping.[35,56,57] Including these effects will change radically the results of calculation for small distances $g<0.5$ nm.

D. Enhancement factors for large prolate spheroids

In Fig. 8 the relative enhancement factors F^2 and D calculated for large nanobodies are represented. One can see a new feature: the F_-^2 factor exhibits deep minima: the longer is the body, the more minima appear in spectra of F_-^2. One can see with increasing length of the spheroids the increase in the first (dipolar) resonance and its shift into the infrared. In Fig. 9 the influence of Bessel beam angle is shown. One can see the radically changed value F_+^2 when the BB angle increases only by 1°, see Figs. 9(b) and 9(c). For $\theta>41.8°$ the ATR regime exists: due to the exponential decay of the field the excitation by plasmons occurs at the "close" body end. For the subcritical BB angles like 10° or 41° we see deep minima in factors F_+^2, which can be attributed to a destructive interference of the exciting Bessel beam with plasmon modes, excited along the whole nanobody length. Similar minima seen on curves of F_-^2, can also be explained via destructive interference of plasmons, excited (for this type of illumination) by a nondecaying external field.

Another interesting effect is seen in Fig. 9(a) for small angles of BB: the relative factors F_+^2 and F_-^2 have much higher values in the region where photon's energy is less than 5 eV (in the visible and near UV). It will be explained below in Sec. IV F.

E. Enhancement factors for STM tiplike nanobody

Light scattering on an aluminum tiplike nanobody is considered. In Fig. 10 the enhancement factors for three nanobodies with equal lengths and volumes, having various shapes and curvatures at the poles are shown. The shapes of these nanotips are described by formulas

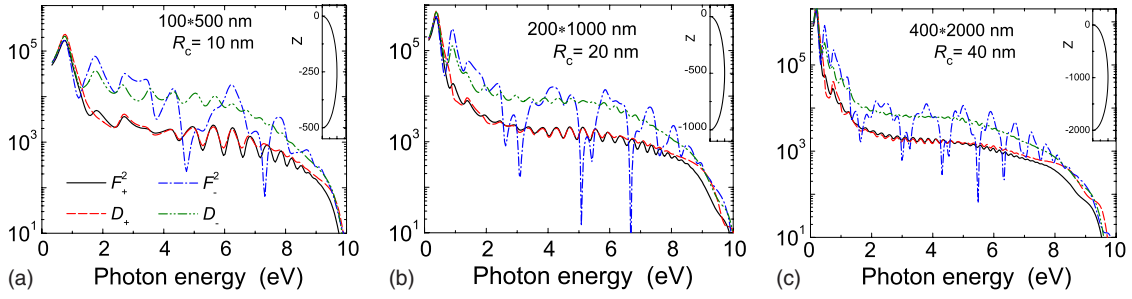

FIG. 8. (Color online) Relative enhancement factors for aluminum prolate spheroids (semicontours are shown in the insets) with aspect ratio 1:5. Spheroids have diameters, lengths, and corresponding curvature radii at the poles R_c, indicated in Fig. 8. The beam angle is $\theta=45°$.

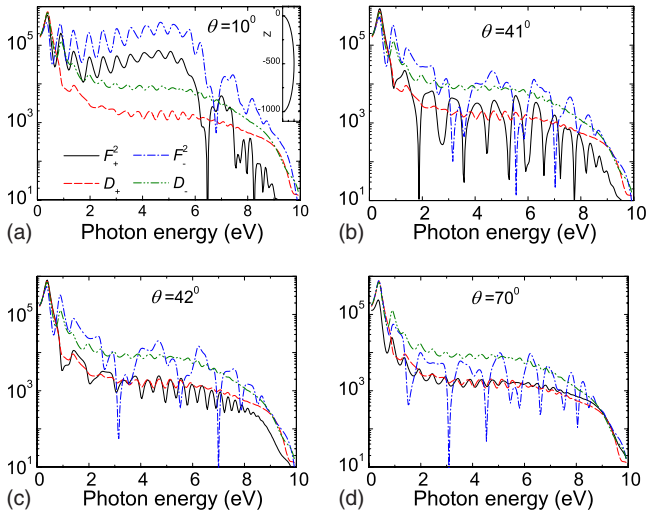

FIG. 9. (Color online) Enhancement factors for aluminum prolate spheroid (200×1000 nm^2) illuminated under various angles of Bessel beam. Note, the D factors are shown by the same curves in all figures due to their independency of BB angle.

$$z - z_0 = b\cos(\psi), \quad r = a\sin(\psi)\sqrt{1-\left(1-R_c\frac{a}{b^2}\right)\cos(\psi)},$$

where a and b are the semiaxis of initial spheroid, ψ is the parameter going from zero to π, z_0 is the center of the spheroid, and R_c is the radius of curvature at the pole, placed close to film surface. Note that for the value $R_c=b^2/a$, we again obtain nondeformed spheroid. A deformed spheroid will be called below a tip.

Interesting features are seen in Fig. 10: (a) the height of the first resonance at low frequencies (the dipolar resonance) is independent of the nanobody's radius of curvature; (b) a small radius of curvature causes an increase in all spectra in

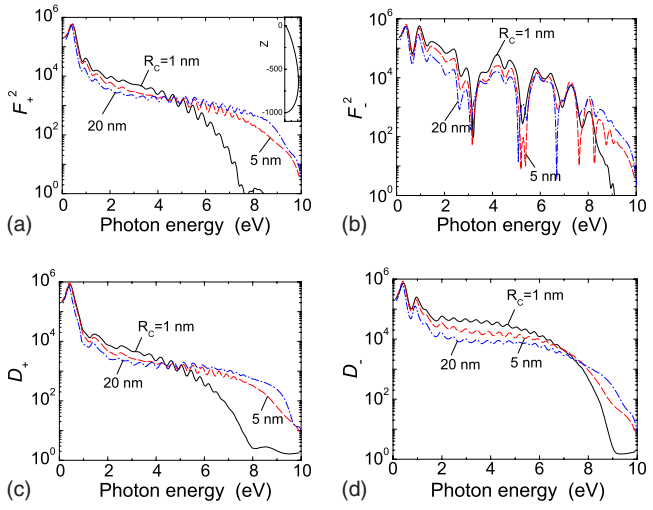

FIG. 10. (Color online) Enhancement factors for aluminum tip (deformed spheroid). Influence of curvature radius. All nanobodies have the same length and volume as the spheroid 200×1000 nm^2. Nondeformed spheroid has the radius of curvature 20 nm. $\theta=45°$; $g=1$ nm; and $h=20$ nm.

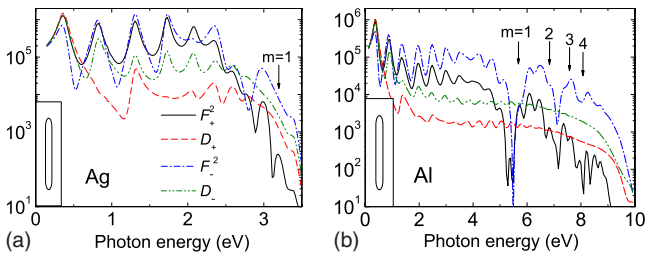

FIG. 11. (Color online) F^2 and D spectra for long (a) Ag and (b) Al nanorods illuminated at BB angle $\theta=10°$. The shape of nanorod is shown in the inset (100×1000 nm^2, $R_c=20$ nm). $g=1$ nm; (a) $h=50$ nm (Ag); (b) $h=20$ nm (Al).

the low-frequency domain ($\hbar\omega<5$ eV for F_+^2 and D_+ and $\hbar\omega<7$ eV for F_-^2 and D_-) and a strong damping in the high-frequency region; (c) the minima positions in the factor F_-^2 [Fig. 10(b)] are not dependent on the nanobody's curvature.

Why does for the ATR configuration [Figs. 10(a) and 10(c)] a decrease in the local radius of curvature lead to a strong damping of enhancement factors for short wavelengths? The reason is that the volume of the NP which is excited by the exponentially decaying near field can be estimated as $V=R_c^2\lambda$, and when R_c is decreasing from 20 to 1 nm one can get a reduction in enhancement factors by two-three orders of magnitude.

F. Enhancement factors for long Al nanorod

Let us consider large NPs of a different shape, the silver and aluminum nanorods, having a length of 1000 nm, a diameter of 100 nm, and ending in spheroidal caps with radius of curvature of 20 nm. Factors F^2 and D are calculated and shown in Fig. 11 (for $\theta=10°$ and $g=1$ nm). Note, that for the silver nanorod we have to use the optical properties collected in the book of Palik,[40] because the data of Johnson and Christy[39] are not continued far enough into infrared. It is well known, that in the visible the imaginary part of the permittivity is very different for these two sets of data. It means, the plasmonic resonances in Ag nanorod seen in Fig. 11(a) could be even higher if other material properties would be used. For a silver nanorod the total enhancement factor F^2D can reach resonant values 10^{11}, if D_- is used.

One can compare curves in the Figs. 9(a) and 11(b) calculated for Al nanobodies of different shapes at the same BB angle 10^0. The curvature radii and lengths for two bodies are the same, but the diameter of the prolate spheroid is twice larger (200 nm) than for nanorod. The decreased surface and volume of the nanorod results in a certain decrease in all enhancement factors. Also the position of the first deep minimum for F_+^2 (and similar for F_-^2) is shifted to a lower value [from 6.4 eV (spheroid) to 5.5 eV (nanorod)]. An interesting feature of these figures is the existence of two domains of photon energies with qualitatively different behavior of F factors. To explain this, we can use quantum notions like momentum of photon and plasmon. It is well known,[46] that a photon with momentum component $\hbar k\sqrt{\varepsilon_e}\cos(\theta)$ parallel to the NP surface cannot excite surface plasmon with momentum $\hbar k\sqrt{\varepsilon_p\varepsilon_e/(\varepsilon_e+\varepsilon_p)}$ (the real part of ε_p is negative and we

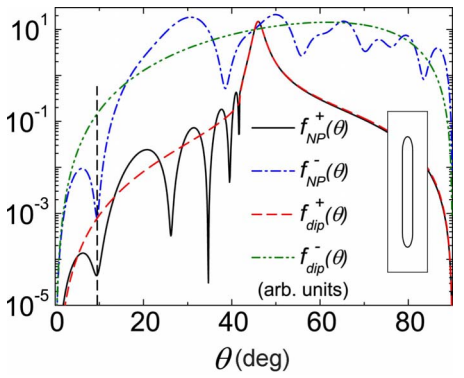

FIG. 12. (Color online) Angular distribution functions (normalized) for NP/dipole/film $f_{\mathrm{NP}}(\theta)$ (solid, dash-dot lines) and for dipole/film $f_{dip}(\theta)$ (dashed, dash-dot-dot lines). Signs "+" and "−" mean dipole radiation directed in upper or lower semispaces, respectively. For better visibility the functions for the lower semispace are multiplied by a factor 100. Nanorod and film are made of aluminum; the gap is 1 nm; the photon energy is 5.5 eV.

ignore its small imaginary part). To avoid this barrier, a surface roughness or artificially grating is made on the smooth metals. We need no grating: thanks to a finite NP length L, there are disturbance modes with wave numbers $m\pi/L$ which can help to fulfill the momentum conservation law

$$\hbar\frac{\omega}{c}\sqrt{\varepsilon_e}\cos(\theta)+\hbar m\frac{\pi}{L}\sqrt{\varepsilon_e}\geq\hbar\frac{\omega}{c}\sqrt{\frac{\varepsilon_e\varepsilon_p}{\varepsilon_e+\varepsilon_p}}$$

or in the final form

$$\cos(\theta)+m\frac{\pi c}{L\omega}\geq\frac{1}{\sqrt{1+\varepsilon_e/\varepsilon_p(\omega)}}. \tag{55}$$

The first root of Eq. (55) for silver is $\hbar\omega_1=3.2$ eV and for aluminum nanorod it is $\hbar\omega_1=5.65$ eV (for NP length $L=1000$ nm and BB angle $\theta=10°$). In Fig. 11 these energies are designated by vertical arrows with $m=1$. For silver all these roots are found in the domain with a high damping and therefore have no influence. For aluminum their positions correlate well with the deep minima domain [see arrows in Fig. 11(b)].

Let us show that the Eq. (55) gives also good results for large angles. Return to Fig. 9(b), and look at the solid curve describing the factor F_+^2 for the case of subcritical BB angle $\theta=41°$. It is not the angle of illumination of NP. When we use the refraction law the illumination angle in the lower subspace is equal 80°. For this angle we get the first root of Eq. (55) is $\hbar\omega_1=0.75$ eV; the second root is $\hbar\omega_2=1.5$ eV. These values are close to the first minima of factor F_+^2 as one can see in Fig. 9(b).

G. Angular distribution functions for dipole radiation: Demonstration of the optical reciprocity theorem (ORT)

In Fig. 12 the angular distribution functions for dipole radiation are shown. These functions are normalized with respect to the radiation integrated over all angles into a semispace. Subscript "NP" in the distribution functions means the

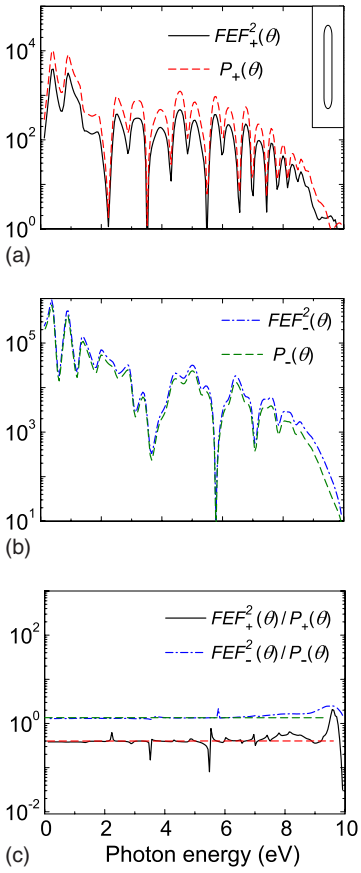

FIG. 13. (Color online) Spectra of field-enhancement factor $\mathrm{FEF}^2(\theta)$ and angular distribution function for dipole radiation $P(\theta)$ calculated by formulas (48) and (49) at the angle $\theta=34.7°$. Light comes from and goes to (a) upper and (b) lower semispaces, respectively; (c)—ratios of the examined values $\mathrm{FEF}^2(\theta)$ and $P(\theta)$.

configuration when dipole and NP are considered, subscript "dip" means the case when only the dipole radiation (without NP) is considered. The photon energy is 5.5 eV, where deep minima in F^2 factors are seen in Fig. 11(b). The angle $\theta=10°$ is indicated in Fig. 12 by a vertical line, where a coincidence of minima of factors F_+^2 and F_-^2 occurs. An interesting feature is demonstrated by the solid and dashed curves, which coincide for angles larger than the critical angle of total reflection (the forbidden sector[46]). It is a consequence of the exponentially decaying factor (discussed in the Sec. III D): the distant parts of the NP are not sending photons into the forbidden sector and the closely situated parts of the NP radiate light in a similar way as a dipole. Alternating maxima and minima seen in the angular distribution functions $f_{\mathrm{NP}}(\theta)$ demonstrate alternating constructive and destructive interference between outgoing radiation and plasmon modes excited in the NP.

Let us demonstrate the ORT. We choose the same NP (Al nanorod). Then we take a certain BB angle, for example, the angle $\theta=34.7°$, where the third deep minimum in the value $f^+_{\mathrm{NP}}(\theta)$ is situated (shown by solid line in Fig. 12). In Figs. 13(a) and 13(b) the spectra of $\mathrm{FEF}^2(\theta)$ and the angular distribution functions for outgoing radiation $P(\theta)$, given by expressions (48) and (49), are shown. These values must be proportional to each other according to the ORT. We can see

in Figs. 13(a) and 13(b) a very complex behavior of the values with many minima and maxima. But in general the ratio of values $\mathrm{FEF}^2(\theta)$ and $P(\theta)$ is constant as it is demonstrated in Fig. 13(c). One can see that the exact proportionality is not much destroyed by the numerical errors which become larger with increasing photon energy. Also in Fig. 13(c) it is seen that the deviations are larger in close vicinity to the sharp minima. It is a quite natural result.

The results shown in Fig. 8–13 were obtained for a number of 200 points distributed along the nanobody's contour. More dense distribution of nodes is used in the gap region. We can conclude that our method of calculation gives results which are in good accordance with the classical theorem of reciprocity. It is very important because it means that the calculated new features—deep spectral minima and a large enhancement for small illumination angles—are not artifacts. But we should recognize that the detailed mechanism of these phenomena is still unclear.

V. DISCUSSION

The axial symmetry, used in our model, can be motivated as follows. We consider axial symmetrical light scattering and light collecting systems posed on the same axis of symmetry. Let's consider a plane p-polarized EM wave coming (as an example) from the lower semispace. The axial component of the electric field in the wave reflected from a layered medium (without NP) can be expressed in cylindrical coordinates by the formula

$$E_z^{(e)} = E_0 \sin\theta [e^{ikz\cos\theta} + R_-(\theta)e^{-ikz\cos\theta}] \sum_{m=-\infty}^{\infty} i^m J_m(kr\sin\theta)e^{im\varphi}, \quad (56)$$

where r, z, and φ are the observation coordinates and E_0, k, θ, and R_- are the wave amplitude, wave number, propagation angle relative to z axis, and the reflection coefficient, respectively. The term with $m=0$, the zero harmonic, described by the Bessel function $J_0(\cdot)$ is the axial symmetrical BB used in our model. Similar decompositions can be built for the other two components of electric field vector.

The EM field scattered by a NP (placed at layered medium) can be also expressed as a decomposition in azimuthal modes

$$\vec{E}' = \sum_{m=-\infty}^{\infty} \vec{E}'_m(r,z)e^{im\varphi}. \quad (57)$$

The electric field on the symmetry axis (at $r=0$) must be a single-valued function of z and hence it must be independent of φ. It means $\vec{E}'_m(r=0,z)=0$ for $m\neq 0$. The same is true for formula (56) because $J_m(0)=0$ for $m\neq 0$. We will use these features later.

Let us describe the elastic scattering cross-section σ following from the formula (57). Substituting the electric field in the Pointing vector $\vec{S}=\frac{c\vec{k}}{8\pi}|\vec{E}'|^2$ and integrating it over the lower semisphere in a far zone yields the energy flux W of scattered light. Dividing this value by the energy-flux density of the illuminating plane wave ($S_0=\frac{ck}{8\pi}E_0^2$) we obtain the elastic cross-section for light scattered into the lower semispace

$$\sigma = \frac{W}{S_0} = \sum_{m=-\infty}^{\infty} \int_0^{\pi/2} \left| \frac{\vec{E}'_m(R,\theta)}{E_0} R \right|^2 2\pi \sin\theta \, d\theta, \quad (58)$$

where the cylindrical coordinates (r, z) are replaced by spherical ones (R, θ) natural for a far zone. This cross-section corresponds to the case when illumination is coming from below and scattered radiation is collected also in the lower semispace. There are three additional cross-sections: one for the radiation scattered into the upper semispace and two for the other illuminating beam coming from above through the support/film. But all these values have structures similar to formula (58): they are sums of positive terms. Therefore the axial symmetrical approach described only by the zero term in Eq. (58) leads to an underestimation of the scattering cross-section.

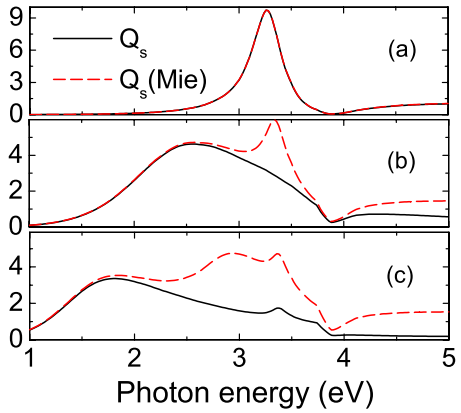

FIG. 14. (Color online) Scattering cross-section efficiency for Ag sphere: full Mie model (dashed line) and axial symmetrical model (solid curve). Spheres diameters are: (a) $2a=80$; (b) 120; and (c) 240 nm.

In Fig. 14 we demonstrate the impact of the higher order azimuthal modes for the exactly solved Mie problem (scattering of plane EM wave on a single sphere). Because in this example the layered medium is absent we can consider integration in formula (58) spanning the full range of scattering angle $0\leq\theta\leq\pi$. The scattering cross-section efficiencies $Q_s=\sigma/\pi a^2$ shown in Fig. 14 for silver spheres of various diameters are calculated at wavelength $\lambda=630$ nm via our axial symmetrical model (solid lines) and by the algorithm for the Mie problem described in the book of Bohren and Huffman[58] (dashed lines). The influence of high modes is very small for spheres with diameters less than reduced wavelength $\lambda\!\!\!^{-}=\lambda/2\pi=99.5$ nm. The larger is the sphere, the more is the difference between the curves, caused by the influence of high harmonics. One can conclude that the approach of axial symmetry can give only a lower estimate for the elastic scattering cross-section. A similar conclusion is valid also for extinction cross-section.[59]

Let us return to Raman (nonelastic) light scattering. This light is emanated by the oscillating dipole and is shifted in frequency. Therefore it cannot interfere with the light de-

scribed by formulas (56) and (57). The single source of Raman signal is the point dipole, placed on the symmetry axis, oriented along the axis, and excited by a sum of the electric fields [Eqs. (56) and (57)]. As it was mentioned previously, the impact of all high azimuthal modes in expressions (56) and (57) disappear at $r=0$. Therefore, the dipole acts like filter of high harmonics: it cuts off all modes with $|m| \geq 1$. Only the azimuthal mode with $m=0$ can excite the dipole. Hence the developed axial symmetrical model of the TERS phenomenon is correct (exact and full).

The used method of calculation is based on the reduction in the Maxwell equations for problems of axial symmetry to a system of one-dimensional boundary integral equations (BIEs). This method is called also as BEM. BIEs method has advantages: (1) decreasing of the dimension of problem; (2) exact matching to the Sommerfeld radiation conditions for fields at infinity; (3) simple accounting for the curvilinear boundary of the scattering particles; and (4) accurate calculations of fields in regions of high curvature of particle's boundary and in narrow domains ("hot spots"). The fields calculated by this method are accurate solutions of Maxwell equations. During long calculations simulating complex physical phenomena it is important to have reliable methods of quality control of calculated results. The exact solution like the Mie problem is very useful for a demonstration of a high accuracy of calculated values in a simple case. But in the complex case as a NP placed near a layered medium we should find other testing procedures. For the accuracy control one can use some exact identities. First, we have used the identities valid for the external illuminating fields (Bessel beam and dipole radiations) as exact solutions of Maxwell equations. This permits us to control the Green's function of the layered medium calculated via complex Sommerfeld[38] integrals. Second, the accuracy of calculated enhancement factors for local field and dipole radiation is proven via the optical reciprocity theorem (ORT). Both methods gave good results: Green's function is calculated with relative errors not larger than 0.1%, and enhancement factors ratios deviate from constant values less than (1–5)% in the regular regions (except the deep minima and the shortest wavelengths). According to ORT these ratios should be exactly constant.

We demonstrate that the gap modes have a strong dependence on the NP-film distance g. For $g \sim 1$ nm the gap electric field can be 10^3 times larger than the field of the illuminating beam. Because these modes can be clearly detected at the opposite pole of a NP, they should be considered as having a global character. Gap modes are distributed over the whole volume, or, more correctly, over the whole surface of a NP. They are much stronger for small NPs with sizes $<\lambda\!\!\!^{-}$, than for large (elongated) NPs. For large NPs the influence of gap modes on the field enhancement is small. A simple electrostatic analogy with a flat capacitor can explain the gap field behavior at small NP-film distances: $\mathrm{FEF} \propto g^{-1}$.

The used BIEs include a Fredholm integral equation of the first kind (relative to a part of unknowns, the normal derivative $\frac{\partial H_\varphi}{\partial \nu}$). Usually this type of integral equations has unstable solutions. But in our case, very stable results due to a phenomenon of self-regularization[60] were obtained. A self-regularization means a presence of large elements in the main diagonal of the global matrix of the system of linear equations. These large elements arise due to the logarithmic singularity in the Green's function. We can conclude from Figs. 7 and 8 that the used BEM gives really stable results of high quality (without numeric noise) for supersmall gaps, which are thousand times less than the NP length. Other methods, based on finite differences, finite elements or series decompositions cannot resolve so accurately the electromagnetic problems with so small gaps.

The enhancement factor of Raman radiation is the product of two factors: a square of a local field-enhancement factor FEF^2 and a DEF. The calculation of values FEF^2 and DEF is fully independent, but is based on the same Green's function. Therefore the resonance frequencies for values FEF^2 and DEF are the same (we ignore the frequency shift in the argument of DEF, caused by oscillating molecule). We introduce the relative factors $F^2=(\mathrm{FEF}/A)^2$ and $D=\mathrm{DEF}/J$, where A is the local field at the dipole position and J is the dipole radiation (both without nanoparticle). By introducing the film-enhancement factor $I=A^2J$ the total enhancement is represented as $\mathrm{REF}=IF^2D$. The film factor I enhances the signal due to plasmon resonance in the film, but it is not a confined field. The light in BB has a spot size, comparable to the wavelength. Therefore we concentrate our attention on the product F^2D as a measure of enhancement caused by NP. The radius of field confinement is usually estimated as $\sqrt{gR_c}$, where g is the NP/film gap and R_c is the local curvature radius of NP.

We consider two field-enhancement factors F_+^2 and F_-^2 when illumination comes under some fixed angle θ from the support or from below, and two factors D_+ and D_- for dipole radiation, which goes in the upper or in the lower semispaces, respectively. Spectra of relative factors F^2 and D demonstrate very close values for NPs with extension in the z direction less than the reduced wavelength $\lambda\!\!\!^{-}=\lambda/2\pi$. The factors coincide for the first (dipolar) resonance because this resonant wavelength is always much larger than the length of NP. It was found in Kretschmann configuration ($\theta > \theta_{cr}$) that there is a strong correlation among the introduced relative factors: $F_+^2 \approx D_+$. Illumination by an evanescent field seems promising due to reducing the background light. But the Kretschmann configuration responsible for F_+ and its inverse configuration of a dipole radiating into the forbidden angles, being responsible for D_+, has a disadvantage for elongated NP. This is connected with an exponentially decaying factor which decreases the contribution of distant parts of the NP to the enhanced field at the dipole position (F_+). A similar exponentially decaying factor decreases the contribution of distant parts of the NP to the radiation into the forbidden angular sector above the film (a part of D_+). These decaying factors decrease the values F_+^2 and D_+ relative to the factors F_- and D_- by one to two orders of magnitude.

Two interesting new features are discovered in our calculations. First, for large NPs and non-Kretschmann illumination some deep minima occur in the field-enhancement factors F_+^2 and F_-^2. This effect depends on the BB angle θ and can be explained as a destructive interference of excited plasmonic modes and the radiation field. It can considerably decrease the total enhancement caused by the NP. Second, for small angles θ in a wide spectral domain for photon energies lower than some threshold level the opposite phenomenon is

seen: the field-enhancement factors F_+^2 and F_-^2 are considerably higher than for large angles of BB. This is demonstrated for a long aluminum prolate spheroid in Fig. 9(a) and for Ag and Al nanorods in Figs. 11(a) and 11(b), respectively. This phenomenon can be explained on the basis of the law of conservation of momentum: the smaller is the angle θ, the better is the momentum matching between exciting photons and excited NP plasmons.

At the gap ~ 1 nm for aluminum prolate spheroid and long nanorod in the visible the product F^2D can be about 10^7-10^9. For small silver and golden spheres this composite factor reach $10^{10}-10^{11}$. This is close to results obtained in Refs. 10, 17, 25, and 33–36. For long nanoparticles, calculated in our work, all dipolar resonances are situated in the infrared and for D and F^2 factors we have obtained here values $\sim 10^6$. For a long silver nanorod at small BB angles and at the resonant frequencies the calculated product F^2D can reach values $10^{10}-10^{11}$. If the additional chemical enhancement factor $\sim 10^2$ is included into our estimation one can get a huge enhancement of Raman signal $\sim 10^{13}$, which is close to the total enhancement factor, found for single-molecule surface enhanced Raman scattering (SM-SERS).[8–10]

We have considered three metals: gold, silver, and aluminum. Each of them has advantages and disadvantages. Gold and silver are often used in SERS and TERS. Aluminum has a high plasmonic activity in a very wide spectral region, from UV to IR. But aluminum is always covered by a hard and thin ($\sim 1-2$ nm) film of oxide. This film not only increases the tip/surface distance but also totally blocks the chemical mechanism of SERS, which is based on overlapping of molecular and atomic orbitals.

VI. CONCLUSION

An axially symmetrical TERS model is developed; solutions of Maxwell equations are calculated by a self-made flexible code based on the boundary element method; a layered medium and metallic nanoparticle made of various materials (gold, silver, and aluminum) with various shapes and sizes, angles of the illuminating beam, and light frequencies are considered; local field and dipole radiation enhancement factors are calculated; the angular distribution function for dipole radiation is derived and the correspondence of obtained results to the known optical reciprocity theorem is shown. At certain frequencies due to destructive interference of plasmonic modes, excited in a long nanoparticle, and external radiation the local field enhancement can be considerably damped. This negative effect can be shifted to the high-frequency domain and field enhancement can be increased by one to two orders by illuminating under small beam angles. In this case, at least for silver and by including chemical enhancement, the total enhancement $\sim 10^{13}$, sufficient for SM-TERS, can be reached.

ACKNOWLEDGMENTS

P. I. Geshev acknowledges support from the German Science Council (DFG). The authors thank Sergey Zimovetz for calculation of data, shown in Fig. 14.

[1] M. Fleischmann, P. J. Hendra, and A. J. McQuillan, Chem. Phys. Lett. **26**, 163 (1974).
[2] D. L. Jeanmaire and R. P. Van Duyne, J. Electroanal. Chem. **84**, 1 (1977).
[3] M. G. Albrecht and J. A. Creighton, J. Am. Chem. Soc. **99**, 5215 (1977).
[4] J. I. Gersten, J. Chem. Phys. **72**, 5779 (1980).
[5] J. I. Gersten and A. Nitzan, J. Chem. Phys. **73**, 3023 (1980).
[6] P. F. Liao and A. Wokaun, J. Chem. Phys. **76**, 751 (1982).
[7] M. Moskovits, Rev. Mod. Phys. **57**, 783 (1985).
[8] S. Nie and S. R. Emory, Science **275**, 1102 (1997).
[9] K. Kneipp, Y. Wang, H. Kneipp, L. T. Perelman, I. Itzkan, R. R. Dasari, and M. S. Feld, Phys. Rev. Lett. **78**, 1667 (1997).
[10] H. Xu, E. J. Bjerneld, M. Käll, and L. Börjesson, Phys. Rev. Lett. **83**, 4357 (1999).
[11] R. M. Stöckle, Y. D. Suh, V. Deckert, and R. Zenobi, Chem. Phys. Lett. **318**, 131 (2000).
[12] M. S. Anderson, Appl. Phys. Lett. **76**, 3130 (2000).
[13] B. Pettinger, G. Picardi, R. Schuster, and G. Ertl, Single Mol. **3**, 285 (2002).
[14] B. Pettinger, B. Ren, G. Picardi, R. Schuster, and G. Ertl, Phys. Rev. Lett. **92**, 096101 (2004).
[15] J. Steidtner and B. Pettinger, Phys. Rev. Lett. **100**, 236101 (2008).
[16] H. Watanabe, N. Hayazawa, Y. Inouye, and S. Kawata, J. Phys. Chem. **109**, 5012 (2005).
[17] M. Futamata and Y. Maruyama, in *Nanoplasmonics: From Fundamentals to Applications*, edited by S. Kawata and H. Masuhara (Elsevier, Amsterdam, 2006), p. 101.
[18] A. Otto, Indian J. Phys., B **77**, 63 (2003).
[19] E. Zeman and G. Schatz, J. Phys. Chem. **91**, 634 (1987).
[20] W.-H. Yang, G. C. Schatz, and R. P. Van Duyne, J. Chem. Phys. **103**, 869 (1995).
[21] M. Kerker, D. S. Wang, and H. Chew, Appl. Opt. **19**, 4159 (1980).
[22] D. S. Wang, H. Chew, and M. Kerker, Appl. Opt. **19**, 2256 (1980).
[23] P. W. Barber, R. K. Chang, and H. Massoudi, Phys. Rev. B **27**, 7251 (1983).
[24] J. Wessel, J. Opt. Soc. Am. B **2**, 1538 (1985).
[25] T. Takemori, M. Inoue, and K. Ohtaka, J. Phys. Soc. Jpn. **56**, 1587 (1987).
[26] U. C. Fischer and D. W. Pohl, Phys. Rev. Lett. **62**, 458 (1989).
[27] Y. Inouye and S. Kawata, Opt. Lett. **19**, 159 (1994).
[28] E. Kretschmann and H. Raether, Z. Naturforsch. **23B**, 2135 (1968).
[29] L. Novotny, M. R. Beversluis, K. S. Youngworth, and T. G. Brown, Phys. Rev. Lett. **86**, 5251 (2001).
[30] A. Bouhelier, J. Renger, M. Beversluis, and L. Novotny, J. Microsc. **210**, 220 (2003).

[31] T. Grosjean, D. Courjon, and D. Van Labeke, J. Microsc. **210**, 319 (2003).
[32] R. Dorn, S. Quabis, and G. Leuchs, Phys. Rev. Lett. **91**, 233901 (2003).
[33] F. Demming, J. Jersch, K. Dickmann, and P. Geshev, Appl. Phys. B: Lasers Opt. **66**, 593 (1998).
[34] P. I. Geshev, S. Klein, T. Witting, K. Dickmann, and M. Hietschold, Phys. Rev. B **70**, 075402 (2004).
[35] P. I. Geshev and K. Dickmann, J. Opt. A, Pure Appl. Opt. **8**, S161 (2006).
[36] P. I. Geshev, U. Fischer, and H. Fuchs, Opt. Express **15**, 13796 (2007).
[37] M. Born and E. Wolf, *Principles of Optics* (Pergamon Press, New York, 1964).
[38] A. Sommerfeld, *Partielle Differentialgleichunge der Physik* (Verlag Geest und Portig, Leipzig, 1948).
[39] P. B. Johnson and R. W. Christy, Phys. Rev. B **6**, 4370 (1972).
[40] E. D. Palik, *Handbook of Optical Constants of Solids* (Academic Press, New York, 1985).
[41] E. V. Zakharov and Yu. A. Eremin, USSR Comput. Math. Math. Phys. **19**, 267 (1979).
[42] K. Sakoda, K. Ohtaka, and E. Hanamura, Solid State Commun. **41**, 393 (1982).
[43] L. Landau, E. Lifchitz, and L. Pitaevskii, *Electromagnetics of Continuous Media* (Pergamon, Oxford, 1984).
[44] E. C. Le Ru and P. G. Etchegoin, Chem. Phys. Lett. **423**, 63 (2006).
[45] W. Lukosz and R. E. Kunz, J. Opt. Soc. Am. **67**, 1615 (1977).
[46] L. Novotny and B. Hecht, *Principles of Nano-Optics* (Cambridge University Press, New York, 2006).
[47] F. J. García de Abajo and A. Howie, Phys. Rev. B **65**, 115418 (2002).
[48] J. Aizpurua, G. W. Bryant, L. J. Richter, F. J. Garcia de Abajo, B. K. Kelley, and T. Mallouk, Phys. Rev. B **71**, 235420 (2005).
[49] U. Hohenester and J. Krenn, Phys. Rev. B **72**, 195429 (2005).
[50] A. M. Kern and O. J. F. Martin, J. Opt. Soc. Am. A Opt. Image Sci. Vis **26**, 732 (2009).
[51] G. E. Forsyte, M. Malcolm, and C. Mouler, *Computer Methods for Mathematical Computations* (Prentice-Hall, New York, 1977).
[52] A. G. Mal'shukov, Phys. Rep. **194**, 343 (1990).
[53] T. Kume, S. Hayashi, and K. Yamamoto, Phys. Rev. B **55**, 4774 (1997).
[54] S. Hayashi, in *Nanoplasmonics: From Fundamentals to Applications*, edited by S. Kawata and H. Masuhara (Elsevier, Amsterdam, 2006), p. 141.
[55] J. A. Porto, P. Johansson, S. P. Apell, and T. Lopez-Rios, Phys. Rev. B **67**, 085409 (2003).
[56] J. Zuloaga, E. Prodan, and P. Nordlander, Nano Lett. **9**, 887 (2009).
[57] I. A. Larkin, M. I. Stockman, M. Achermann, and V. I. Klimov, Phys. Rev. B **69**, 121403(R) (2004).
[58] C. Bohren and D. Huffman, *Absorption and Scattering of Light by Small Particles* (Wiley, New York, 1983).
[59] P. I. Geshev and S. V. Zimovetz, Eng. Phys. **3**, 42 (2009) (in Russian).
[60] V. I. Dmitriev and E. V. Zakharov, *Integral Equations in Boundary Value Problems of Electrodynamics* (Moscow University Press, Moscow, 1987) (in Russian).